ADVANCED FUNCTIONAL MATERIALS
www.afm-journal.de

Micro and Nanostructural Diversity of Lizard Osteoderm Capping Tissue in Relation to Mechanical Performance

*Adrian Rodriguez-Palomo, Marius Didziokas, Malene Siri Berg Jacobsen, Thorbjørn Erik Køppen Christensen, Innokenty Kantor, Mads Ry Vogel Jørgensen, Klaus Pagh Almtoft, Jesper Skovhus Thomsen, Anthony Herrel, Catherine J.A. Williams, and Henrik Birkedal**

This paper is dedicated to the memory of Prof. Helmut Cölfen.

Hard tissues in biology are typically hierarchical composites. Osteoderms are mineralized dermal structures, widespread in lizards, in which a hyper-mineralized superficial layer, the capping tissue, has recently attracted attention for its unusual structural and mechanical features, with, e.g., moduli reaching those of enamel. Here, a comparative study of osteoderms from six lizard species whose osteoderms bear capping tissue (*Heloderma horridum*, *Pseudopus apodus*, *Broadleysaurus major*, *Corucia zebrata*, *Tiliqua scincoides*, and *Tiliqua rugosa*) are presented using X-ray computed tomography, nanoindentation mapping, synchrotron X-ray diffraction/fluorescence imaging, and finite element modeling. The capping tissue is consistently more mineralized than the underlying bone across all species. Mechanical testing shows that the capping tissue is stiffer and harder than bone, but its mechanical properties range widely, from values only slightly exceeding those of bone to enamel-like levels. Two extreme architectures are observed: *H. horridum* and *B. major* exhibit unusually large, near-isotropically arranged crystals and exceptional stiffness, while the other species display smaller crystals, are more textured than bone, and have less extreme stiffness. This demonstrates that capping tissue is a morphologically and functionally diverse specialization, highlighting its potential role in the evolutionary adaptation of osteoderms.

1. Introduction

Hard tissues in vertebrates, such as bone and teeth, are paradigmatic examples of biomineralized tissues acting as natural composite materials. Their outstanding mechanical performance arises not only from the intrinsic properties of their constituents (biomineral nanoparticles and collagen fibers), but also from the way organic and inorganic building blocks are combined into hierarchical architectures across multiple length scales.[1,2] Collagen provides a tough and deformable scaffold, while hydroxyapatite crystals bring stiffness and hardness. Through controlled mineralization of collagen fibrils and organization of crystallites, nature makes composites that achieve an optimized balance of strength, toughness, and functional specialization.[3–5]

This principle is exemplified in several mineralized tissues. Bone and dentin, with a balanced mineral-to-organic ratio,

A. Rodriguez-Palomo, M. Didziokas, M. S. B. Jacobsen, M. R. V. Jørgensen, H. Birkedal
Department of Chemistry and Interdisciplinary Nanoscience Centre (iNano)
Aarhus University
Aarhus 8000, Denmark
E-mail: hbirkedal@chem.au.dk

T. E. K. Christensen, I. Kantor, M. R. V. Jørgensen
MAX IV Laboratory
Lund University
Lund 22594, Sweden

T. E. K. Christensen
DTU Compute
Danish Technological University
Kongens Lyngby 2800, Denmark

I. Kantor
DTU Physics
Danish Technological University
Kongens Lyngby 2800, Denmark

K. P. Almtoft
Tribology Centre
Danish Technological Institute
Aarhus 8000, Denmark

J. S. Thomsen
Department of Biomedicine
Aarhus University
Aarhus 8000, Denmark

The ORCID identification number(s) for the author(s) of this article can be found under https://doi.org/10.1002/adfm.202526169

DOI: 10.1002/adfm.202526169

rely on the intrafibrillar and extrafibrillar mineralization of collagen to provide stiffness while retaining fracture resistance.[6–8] Enamel represents the other extreme: almost fully mineralized, it is built from very large and highly organized bioapatite crystallites that yield exceptional hardness and wear resistance.[6–8] Similar strategies have been observed in the enameloid of parrotfish teeth, which achieve remarkable grinding capacity through dense bundles of highly ordered crystallites,[9] while the enamel-like structures found on the crayfish mandible[10] and both ganoid[11] and elasmoid[12] fish scales combine mineralized layers with collagen-based cores to produce lightweight yet highly protective exoskeletal shields.[13] Across these systems, the synergy of simple building blocks, structured hierarchically, allows vertebrates to produce materials that far exceed the performance of their individual components for both functional and protective purposes.

In terms of protection, the skin is commonly regarded as the primary barrier layer for any vertebrate, separating the organism from its environment. Among the skin's many roles and included in the varied anatomical features that meet these needs, many taxa include mineralized structures in the skin. These are placed variably within the depth of the skin tissue, from superficial in the case of scales,[11,12,14,15] to deep in the dermis.[16–19] In tetrapods, osteoderms are the dominant form of such skin adaptations. Osteoderms are dermal (skin) skeletal structures that are phylogenetically, ecologically, and functionally variable. These structures are common in lizards and are observed sparsely in snakes,[20] mammals,[19] but almost universally in crocodilians and chelonians (aquatic and terrestrial turtles).[16,17]

An increasing number of lizard osteoderms have been reported to bear a superficial layer that differs from the underlying bone in mechanical properties and histological characteristics – the capping tissue. Capping tissue was first described in a species of fossil anguimorph as "osteodermine"[21] and characterized in the extant *Heloderma suspectum*.[22] Recent histological studies on the capping tissue of a wide phylogenetic range of species showed that capping tissue might be more diverse than previously thought.[23] In general, capping tissue is described as collagen and cell-poor. While some species present no apparent staining, as is the case with the *Heloderma spp*., others stain as basophilic tissue, as is the case for the *Tiliqua spp*.[23] More general morphological investigations on the overall osteoderm shape in different lizard species, including nanoindentation in isolated regions, showed that capping tissue is, on average, stiffer than the underlying bone.[18,24,25] However, the composition, nanostructure, and detailed mechanical properties of the capping tissue have not been studied, and a systematic comparison of the capping tissue properties across species is lacking.

The hierarchical micro- and nanostructure of the osteoderm's capping tissue was studied, for the first time, in *Heloderma horridum* by the current authors.[26] *Heloderma horridum* has a hypermineralized capping tissue with marginal collagen content and is enriched in strontium compared to the underlying bone. The biomineral fraction is composed of hydroxyapatite nanocrystals of elongated shape and an anomalously large size, reminiscent of the crystallite sizes found in enamel. Enamel characteristically presents a very high degree of texturing of the mineral phase.[6,7,9,27] Surprisingly, in *H. horridum* capping tissue, the nanocrystals appear to be arranged in a near-isotropic fashion at the micrometer scale, resulting in a hyper-mineralized tissue with a very low degree of crystallographic texture. This nanostructure is uncommon for highly mineralized tissue with high mechanical performance, yet *H. horridum* has the stiffest capping tissue reported for lizard osteoderms to date. The capping tissue meets the underlying bone through a graded interface with a decreasing degree of mineralization, which may help dissipate stress at the interface.

To assess the potential for capping tissue to display these highly unusual characteristics across a phylogenetically and ecologically diverse range of lizards, we studied osteoderm nanostructure and fine-scale material properties in a range of lizard species. We chose a number of species that differ in osteoderm size, degree of mineralization, and habit to cover capping tissue design broadly to identify common architectures and structures. Surprisingly, we find that the capping tissue nano- to microstructures vary tremendously between species, suggesting adaptations that, through diverse mechanisms, converge on similar functional characteristics.

2. Results and Discussion

We compare osteoderms from six different lizard species (**Figure 1**; Figure S1, Supporting Information), namely *Heloderma horridum*, *Pseudopus apodus*, *Broadleysaurus major*, *Corucia zebrata*, *Tiliqua scincoides*, and *Tiliqua rugosa*, to better understand the hyper-mineralized layer of tissue covering the osteoderm bone, referred to as the capping tissue. We present new data on the mineralized osteoderm structure for *P. apodus*, *B. major*, *C. zebrata*, *T. scincoides*, and *T. rugosa*. Previously published data on *H. horridum* were obtained from an open-access repository for comparison with the other species.[26] The species included in this study inhabit different habitats in America, Europe, Africa, Asia, and Oceania, and offer a broad range of osteoderm shapes and sizes.

A. Herrel
Mécanismes Adaptatifs et Evolution
UMR 7179
Muséum national d'Histoire naturelle CNRS
Paris 75005, France
A. Herrel
Department of Biology
Evolutionary Morphology of Vertebrates
Ghent University
Ghent 9000, Belgium
A. Herrel
Functional Morphology Laboratory
Department of Biology
University of Antwerp
Antwerp 2610, Belgium
A. Herrel
Naturhistorisches Museum Bern
Bern 3005, Switzerland
C. J. Williams
Department of Animal and Veterinary Sciences
Aarhus University
Tjele 8830, Denmark
C. J. Williams
Aarhus Institute for Advanced Studies
Aarhus University
8830, Denmark

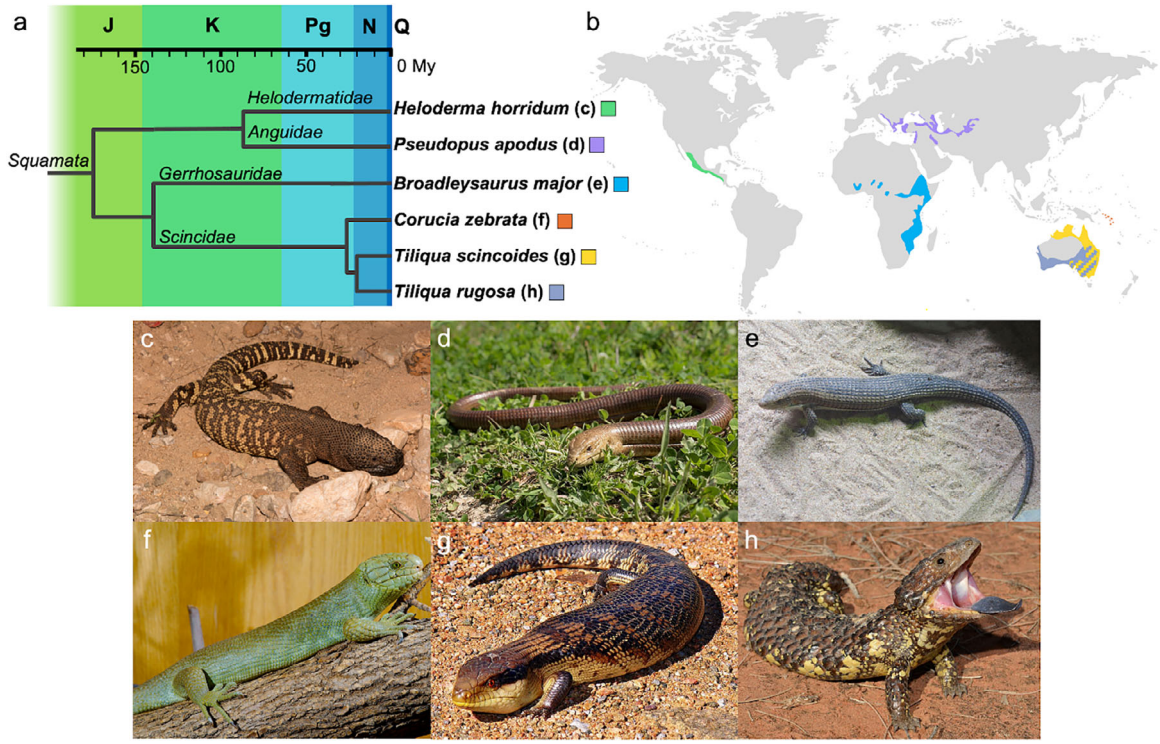

Figure 1. Overview of the lizard species included in this study. a) Phylogenetic tree for species of interest,[25] with periods labeled as J: Jurassic, K: Cretaceous, Pg: Paleogene, N: Neogene, Q: Quaternary. b) Approximate distribution in the present time.[28–33] Photographs of the species (c) *Heloderma horridum*, d) *Pseudopus apodus*, e) *Broadleysaurus major*, f) *Corucia zebrata*, g) *Tiliqua scincoides*, and h) *Tiliqua rugosa*. Photograph credit to (c) Andrew DuBois (CC-BY-NC 2.0), (d) Konstantinos Kalaentzis (CC-BY-SA-4.0), (e) Erlend Bjørtvedt (CC-BY-SA), (f) Guppiecat (CC-BY-NC-ND-2.0), (g) Benjamint444 (CC-BY-SA-3.0), (h) Will Brown (CC-BY-2.0).

2.1. Osteoderm Morphology

We characterize the overall osteoderm shape, size, and morphology by X-ray computed tomography as illustrated in Video 1 and **Figure 2**. The hyper-mineralized capping tissue can be identified as the lighter (higher X-ray absorption) region. There is a large diversity in morphology, contrasting the relatively simple osteoderms from *H. horridum* (Figure 2a), *P. apodus* (Figure 2d), *B. major* (Figure 2g), and *T. rugosa* (Figure 2p) to the compound osteoderms observed in *C. zebrata* (Figure 2j) and *T. scincoides* (Figure 2m). Furthermore, the osteoderms from *H. horridum* are isolated from each other in the dermis, while the osteoderms from the other species present an imbricated structure where the overlapping region can be identified as the flat surface on the dorsal-coronal side (Figure 2d,g,j,m). An exception to this feature is the osteoderm in *T. rugosa*, which, even though imbricated, does not show the same morphology in the overlapping region as the other species (Figure 2p). The *H. horridum* osteoderms have an oblate shape and a knobby surface on the dorsal side and a central vertical neurovascular canal within a channel that branches up to the dorsal surface (Figure 2b,c). In contrast, the rest of the species present a flattened shape, curved in the transverse plane (Figure 2e,h,k,n,q) with a knobby dorsal surface in *P. apodus*, *B. major*, and *T. rugosa*, and a tessellated area with indents in *C. zebrata* and *T. scincoides*. Large channels traverse the osteoderm horizontally in *P. apodus* and vertically in *T. rugosa*, as observed in *H. horridum*.

Video S6 (Supporting Information) shows X-ray computed tomography 3D renderings of an osteoderm from *Heloderma horridum* (voxel size: 1.5 µm), *Pseudopus apodus* (voxel size: 3.8 µm), *Broadleysaurus major* (voxel size: 4.5 µm), *Corucia zebrata* (voxel size: 5.5 µm), *Tiliqua scincoides* (voxel size: 5.8 µm), and *Tiliqua rugosa* (voxel size: 5.5 µm).

The capping tissue, covering the dorsal side of the osteoderms, presents a higher density because it is heavily mineralized,[24] and is visibly more compact on the 10–100 µm scale than the underlying bone, as shown in the virtual sections of the osteoderms in Figure 2. The degree of mineralization in the capping tissue, calibrated using water and hydroxyapatite phantoms, is shown in the violin plots in Figure 2s. The mineral density of the osteoderm bone lies within regular values for such tissue, with a hydroxyapatite content of 1.1–1.4 g cm^{-3};[34] however, not all species present the same mineral density, as the osteodermites from the compound osteoderms in *C. zebrata* and *T. scincoides*, have the lowest mineralized bone tissue. *H. horridum* has the most mineralized capping tissue with a mineral content centered around 1.86 ± 0.09 g cm^{-3}, nearly as much as enamel (2.1–2.3 g cm^{-3}),[35] followed by *T. rugosa* and *B. major*, although the capping tissue in *B. major* is very scarce and therefore it contributes poorly to the total counts in the violin plot. Capping tissue has been previously observed in histological sections[36] to be very poor in collagen in *P. apodus*,[24] and it showed nearly no staining in *H. horridum*[26] and *H. suspectum*.[37] The thickness of the capping tissue varies greatly from a continuous mineralized layer in *H. horridum*, *C.*

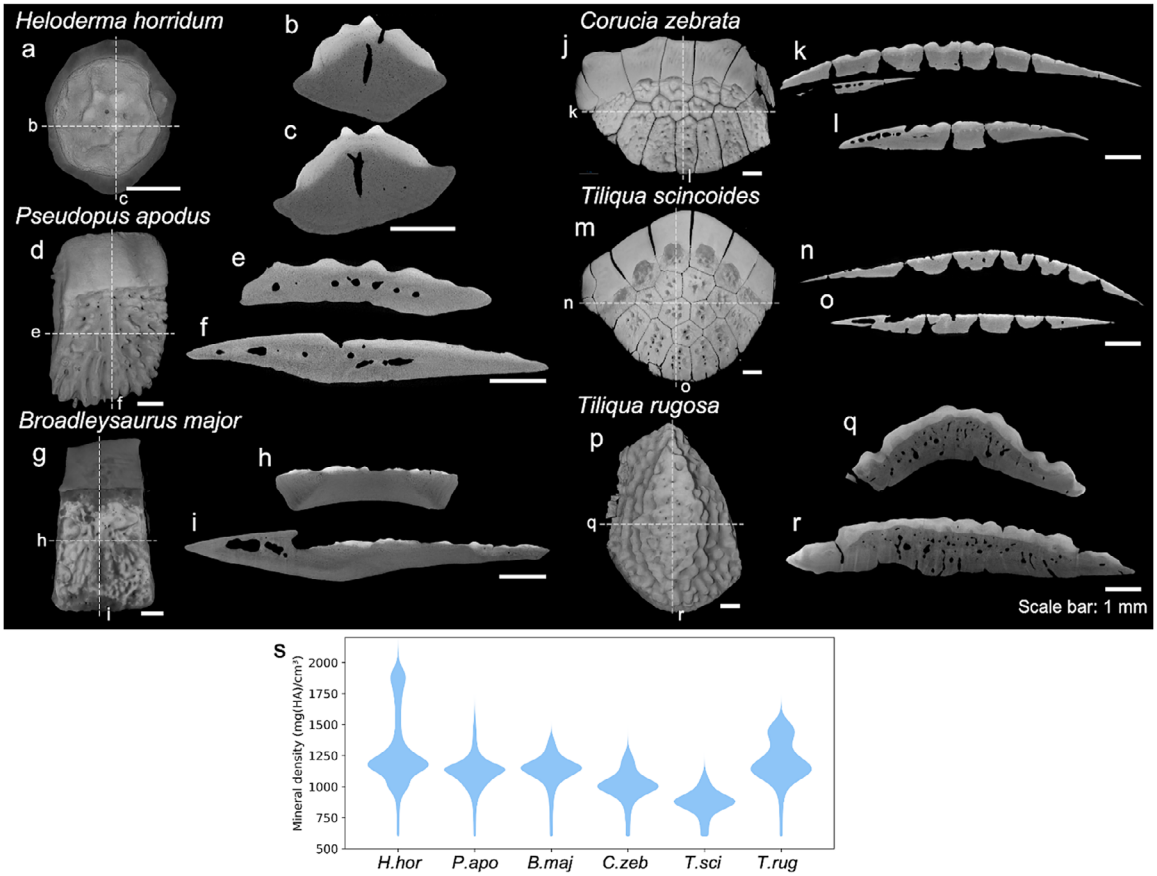

Figure 2. Osteoderm morphology and microstructure. X-ray computed tomography 3D renderings and virtual slices in the (b,e,h,k,n,q) transverse and (c,f,l,l,r) longitudinal planes of an osteoderm from (a–c) *Heloderma horridum* (Video S1, Supporting Information; voxel size: 1.5 µm), d–f) *Pseudopus apodus* (Video S2, Supporting Information; voxel size: 3.8 µm), g–i) *Broadleysaurus major* (Video S3, Supporting Information; voxel size: 4.5 µm), j–l) *Corucia zebrata* (Video S4, Supporting Information; voxel size: 5.5 µm), m–o) *Tiliqua scincoides* (Video S5, Supporting Information; voxel size: 5.8 µm), and p–r) *Tiliqua rugosa* (Video S6, Supporting Information; voxel size: 5.5 µm). Dashed lines indicate the location of the longitudinal (vertical line) and transverse (horizontal line) virtual sections. The 3D renderings are positioned with the cranial-caudal direction in the vertical axis and longitudinal virtual slices with the cranial direction on the left. s) Violin plots of the X-ray CT reconstruction of mineral density as mg of hydroxyapatite per cm^3 for each species with mean values in Table S1 (Supporting Information).

zebrata, *T. scincoides*, and *T. rugosa*, to a more discontinuous layer of isolated hyper-mineralized regions in *P. apodus* and *B. major*. Interestingly, the interface between the capping tissue and the bone also differs strongly between species. In *H. horridum* and *P. apodus*, a relatively wide graded interface is present, previously denoted as the "transition zone", whereas in *B. major*, *C. zebrata*, *T. scincoides*, and *T. rugosa*, the capping tissue-bone interface is more abrupt.

2.2. Mechanical Properties of Capping Tissue and Osteoderm Bone

Capping tissue has previously been reported as being stiffer and harder than the underlying bone.[17,18,22,24] To reveal spatial trends in mechanical properties and compare across species, we use nanoindentation mapping to investigate the local mechanical properties in steps of 10 µm between indents in the longitudinal cross-sections of two different individuals of each species, as shown in **Figures 3** and S2 (Supporting Information). For the compound osteoderms of *C. zebrata* and *T. scincoides*, two different ROIs were selected in each osteoderm to account for variability between each osteodermite. Additionally, the capping tissue and bone regions were visually segmented using optical microscopy. The mechanical properties of each tissue type are displayed in the violin plots in Figure 3m, while mean values are given in the Table S2 (Supporting Information).

The reduced elastic modulus (E) and hardness (H) of the osteoderm bone tissue agree with previously reported values in the literature taken on restricted regions compared to the present large-scale nanomechanical mapping on four of the six species studied herein.[18,24] The measured values in the present study for bone show a mean elastic modulus between 13 ± 3 GPa in *T. scincoides* and 26 ± 5 GPa in *T. rugosa*, and a mean hardness between 0.3 ± 0.1 and 0.9 ± 0.3 GPa in the same species. The local mechanical properties of the capping tissue are significantly larger than those of bone in all species; however, their values vary greatly. The previously reported *H. horridum* has the stiffest capping tissue to date, with mean E = 69 ± 13 GPa and H = 3.2 ± 0.8 GPa, and local values up to E = 95 GPa, H = 5.3 GPa.[26]

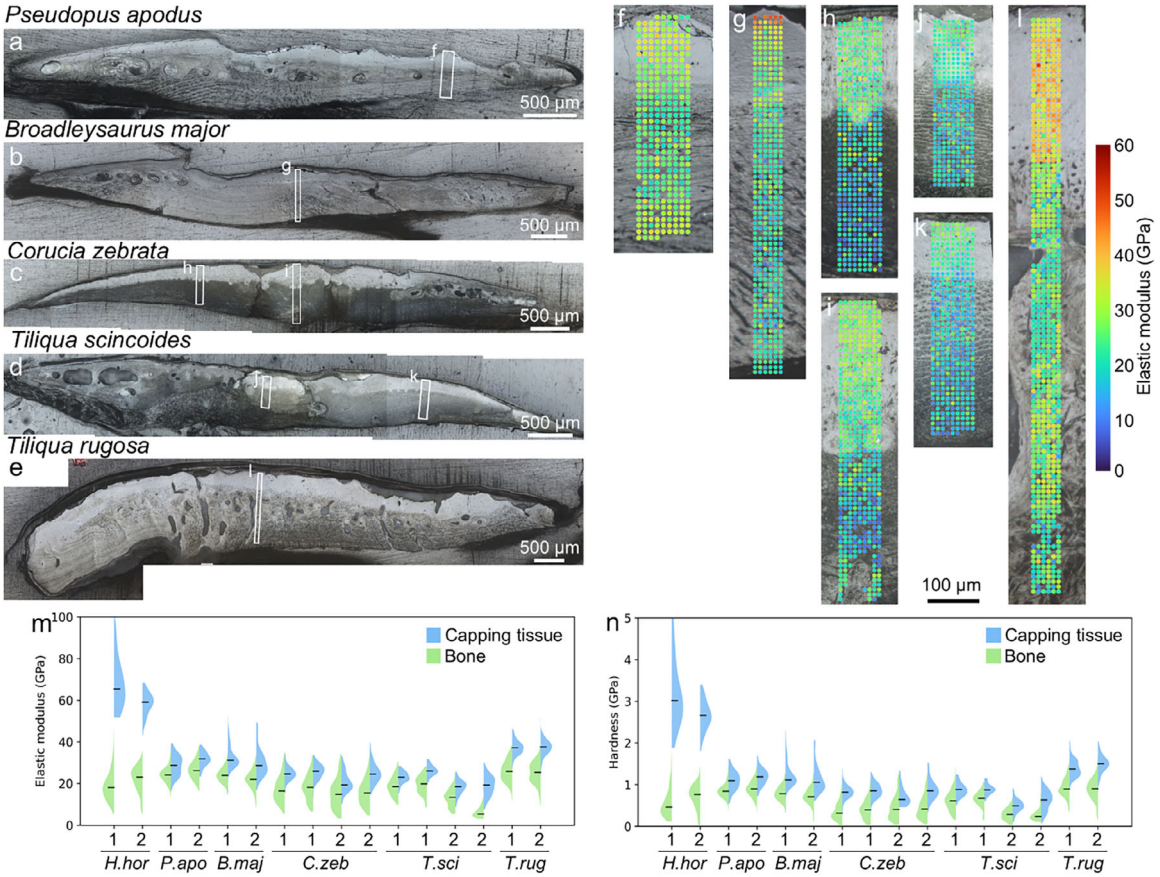

Figure 3. Nanomechanical properties of the lizard osteoderm longitudinal cross-section. a–e) Optical microscopy images of osteoderm cross-sections. The rectangles mark the ROIs used for nanoindentation mapping. f–l) Nanoindentation mapping in steps of 10 µm showing the elastic modulus in each osteoderm. Replicas of the nanoindentation maps in a second individual for each species are shown in Figure S2 (Supporting Information). Panels f-l present species in the same order as in Figure 2a–e. m, n) Violin plots of the elastic modulus and hardness for the capping tissue and osteoderm bone with mean values in Table S2 (Supporting Information). All bone-capping tissue comparisons within each species show statistically significant differences between the two tissues, $p < 0.001$ (see Tables S7 and S8, Supporting Information).

Large E and H are also found in the capping tissue of *B. major* (Figure 3b,g) and *T. rugosa* (Figure 3e,l) with $E = 33 \pm 6$ GPa, $H = 1.2 \pm 0.3$ GPa, and $E = 37 \pm 4$ GPa, $H = 1.5 \pm 0.2$ GPa, respectively. While this is significantly higher than the corresponding values of bone, E and H are much lower than in *H. horridum*, indicating a striking inter-species variation in the mechanical performance of capping tissue. Furthermore, previous data agree with the values for the elastic modulus and hardness of species such as *B. major*,[18] *C. zebrata*,[24] and *P. apodus*.[24] However, the average values alone do not reflect the true microstructure and mechanical properties; the present mapping of mechanical properties reveals a more complex spatial distribution. *Broadleysaurus major* presents high mechanical properties in the upper surface of the osteoderm with values of the elastic modulus and hardness of up to $E = 49$ GPa and $H = 2$ GPa, which decrease to the values of bone when moving across the osteoderm cross-section (Figure 3g). In contrast, *Tiliqua rugosa* has more homogeneous mechanical properties in the capping tissue and bone, even if we observe small variations around structural features in the osteoderm bone, such as pores and areas of higher density (Figure 3l). The mechanical properties of the *P. apodus* capping tissue display values that are higher than those of bone (mean $E = 32 \pm 4$ GPa, $H = 1.2 \pm 0.2$ GPa); however, with a much smaller difference to bone than in the previously mentioned species. Interestingly, nanoindentation mapping shows that the mechanical properties in the bone increase toward the ventral surface where one osteoderm overlaps with the next, indicating adaptation in bone to the imbricated structure (Figure 3f). The capping tissue of the compound osteoderms from *C. zebrata* and *T. scincoides* is stiffer than the osteoderm bone, but the values are only slightly larger than the overall osteoderm bone elastic modulus and hardness, with mean $E = 26 \pm 4$ GPa, $H = 0.9 \pm 0.2$ GPa, and $E = 26 \pm 3$ GPa, $H = 0.9 \pm 0.1$ GPa, for each species, respectively. Additional nanoindentation maps on a second individual can be seen in the Figure S2 (Supporting Information), and the complete list of mean elastic moduli and hardness values for all nanoindentation maps is found in the Table S2 (Supporting Information).

The nanoindentation results thus demonstrate a remarkable diversity in the mechanical performance of capping tissue between species, ranging from enamel-like to only slightly above bone. The large variations in the mechanical properties could suggest adaptations to behavioral interaction, as intra-species aggression has been reported in the case of *H. horridum*[38] and related species.[39,40] This hypothesis, however, does not seem

plausible for all species: Bite force in multiple species correlates with body size,[40] but the mechanical properties of the osteoderms reported here do not. From the mechanical properties reported herein, *Tiliqua* species present very different mechanical properties from *Heloderma spp*., but the two species have very similar bite forces.[25] Similarly, *C. zebrata*, which appears to have a strong bite force in comparison to the other species,[25] has osteoderms with a low E and H in the capping tissue. In contrast, *B. major*, which presents high E and H in our experiments, has been reported to have a much lower biting force than both *Tiliqua spp*. and *C. zebrata*.[25] This speaks to the emergence of both osteoderms and biting performance as under anatomical and selective constraints and under tradeoffs from environment and ecology, and not purely correlated with each other. Hence, the mechanical performance of the osteoderms may arise then as an adaptation, beyond just to conspecifics or predators, but to a wider environment, and reflects the current breadth of hypotheses of osteoderm function more widely.[41]

2.3. Capping Tissue Mineral Nanostructure

To understand the large variations in the microstructural mechanical properties, we studied the nanostructure of the tissues. For that purpose, we used scanning X-ray diffraction and fluorescence microscopy on thin longitudinal and transverse osteoderm slices from one osteoderm per species using a 17 keV X-ray beam and steps of 20 × 10 µm (horizontal × vertical) at the DanMAX beamline at the MAX IV synchrotron (Sweden). The capping tissue and bone areas in the scanning maps were segmented based on tissue density using X-ray radiography of the same slices (Figures S3 and S4, Supporting Information). The resulting masks were used to quantify the different parameters obtained in the analysis, shown in the violin plots below each figure.

Strontium and zinc maps were obtained from the scanning X-ray fluorescence data due to their role in biomineralization as biomarkers in mineral formation.[42,43] The distribution of these oligo elements in the osteoderm is shown in **Figure 4**. The strontium maps show that it is predominantly higher in the capping tissue than in the bone, as also shown in the violin plots in Figure 4f. The distribution of Sr is not homogeneous, though, and, except for the *P. apodus* osteoderms, strontium appears patterned in bands of higher concentration in the capping tissue and bone, especially in the case of *B. major*, *T. scincoides*, and *T. rugosa*, where it is also concentrated on the osteoderm surface. The zinc concentration is higher in the capping tissue than in the bone (Figure 4g); however, it shows a different spatial distribution from that of strontium. Zinc is more concentrated in the capping tissue of *P. apodus*, *B. major*, and *C. zebrata* with respect to the bone than in both *Tiliqua* species. Zinc is also accumulated on the osteoderm surface of all species except *B. major* and some areas of *P. apodus*. The accumulation of zinc at the osteoderm surface may be assigned to either of two opposing phenomena. Zinc accumulation is observed at sites of bone formation in other animals, such as mice,[44] rats,[45] and cows,[46] suggesting that there may be an ongoing active mineralization process taking place at the osteoderm surfaces. However, zinc is also known to be concentrated at cement lines and tide lines at the bone/cartilage interface.[47,48] Further work is required to establish exactly which biological role zinc plays in the context of osteoderms.

The nanostructure of the capping tissue mineral building blocks was studied by scanning X-ray diffraction microscopy experiments and subsequent Rietveld refinement of the integrated diffraction data at each point in the 2D maps.[49] The following section presents the results on the longitudinal slices. The equivalent results of the transverse slices from an additional osteoderm from the same individuals are displayed in the Supporting Information, where similar trends were observed. No significant slice orientation artefacts were observed.

Rietveld refinement of the diffraction patterns in the capping tissue revealed that the mineral phase is entirely composed of biological apatite in all five species studied, in agreement with our previous observations for *H. horridum* capping tissue.[26] The refinement scale factor (Figure S6 (Supporting Information)), which is proportional to the number of unit cells in each scanning point volume, largely coincides with the reconstructed grayscale values in the computed tomography experiments in Figure 2. This confirms the higher degree of mineralization in the capping tissue than in the underlying bone tissue, and the results previously published for the capping tissue of other lizard species.[17,21,22] Maps of the refined unit cell parameters for the a and c-axis are shown in the Figures S7 and S8 (Supporting Information); average values and standard deviations are reported in Table S5 (Supporting Information). To facilitate comparisons, the cell parameters are presented in **Figure 5** using a diverging color scale to show the deviation from the mean value for each thin slice. The lattice constants vary systematically within both bone and capping tissue in manners that, we suggest, reflect the complicated chemical substitution chemistry of apatites combined with strain-inducing interactions between organic and inorganic components. The unit cell a-axis in the capping tissue tends in most cases to be lower than in the osteoderm bone; except for *C. zebrata* (Figure 5c), for which the capping tissue tends to present higher a-axis values, see also Figure 5p that compares the data through violin plots. In the case of *T. rugosa* (Figure 5e), the capping tissue is homogeneously lower in the a-axis than in the rest of the bone, delineating the interface between capping tissue and bone previously seen in the X-ray absorption in Figure 2r. The unit cell c-axis displays two distinct classes of behavior (Figure 5f,g). *H. horridum* and *B. major* capping tissue have a larger lattice c-axis than the bone (see Table S9, Supporting Information for full statistical comparisons). In contrast, the remaining species show the opposite trend with a slightly, but significantly, smaller capping tissue c-axis value in the case of *C. zebrata*, and much lower values in *P. apodus* and both *Tiliqua* species (*T. scincoides* and *T. rugosa*). This result indicates systematic and clear differences between the species, dividing them into two nanostructural groups. Furthermore, we note that the surface of the bone tissue in the overlapping regions of the imbricated osteoderms has a larger a-axis and smaller c-axis than the rest of the osteoderms, especially noticeable in the *P. apodus*, *T. scincoides*, and *T. rugosa*.

The hydroxyapatite crystallite size was calculated using Scherrer's equation from the peak profile parameters obtained in the Rietveld refinement at each scanning point. **Figure 6** shows the

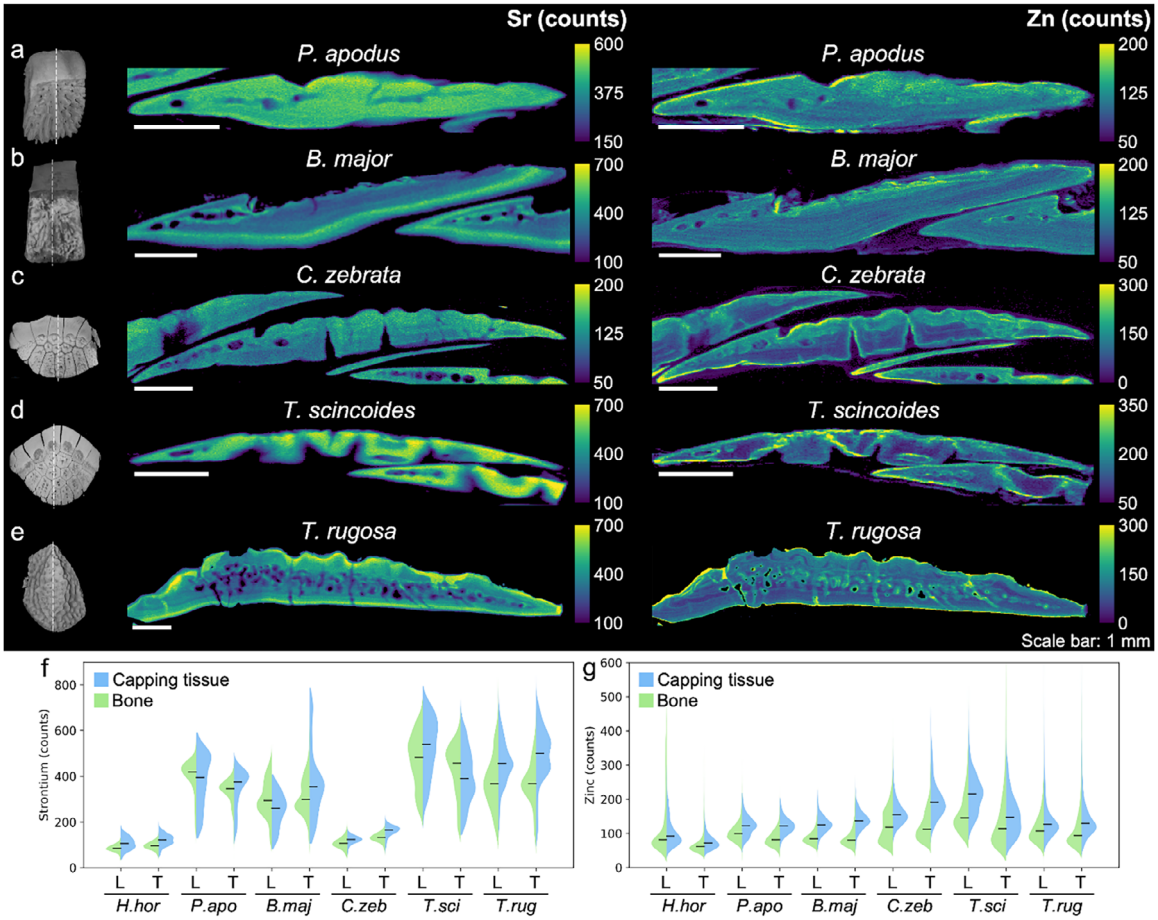

Figure 4. Strontium and Zinc maps of osteoderm longitudinal slices. Tomography 3D renderings and X-ray fluorescence scanning maps for (a) *Pseudopus apodus*, b) *Broadleysaurus major*, c) *Corucia zebrata*, d) *Tiliqua scincoides*, and e) *Tiliqua rugosa*. f, g) Violin plots summarizing the (f) strontium and (g) zinc content in the capping tissue and bone in the longitudinal (*L*) and transverse (*T*) slices for the species of interest, with mean values in Table S3 (Supporting Information). All bone-capping tissue comparisons within each measurement show statistically significant differences between capping tissue and bone, $p < 0.001$ (see Tables S9 and S10, Supporting Information). The approximate location of the thin slice is indicated on the 3D renderings in dashed lines. Note that the osteoderm slices were not obtained from the same osteoderm displayed in the left-side panel. Additional scanning maps on the transverse cross-section can be found in the Figure S5 (Supporting Information).

size of the biomineral nanocrystals in the direction parallel (reflection (002)) and perpendicular (reflection (310)) to the unit cell *c*-axis, which can be approximated to the crystal's length and width. The biomineral crystallite size in the osteoderm bone presents a relatively homogeneous size distribution across all species, with mean values between 27 ± 2 and 36 ± 4 nm in length, and 4.6 ± 0.2–6.0 ± 0.5 nm in width. The bone tissue in *P. apodus* and *C. zebrata* presents some inhomogeneities in the crystallite size with a band below the capping tissue interface. The capping tissue, in stark contrast to bone, displays a striking variation across the five species in this study, and the previously studied *H. horridum*, included in the quantification in Figure 6f,g. As previously seen in the unit cell *c*-axis, the crystallite size in the capping tissue can be divided into two groups. On the one hand, *H. horridum* and *B. major* (Figure 6c) have capping tissue formed by unusually large crystals with mean lengths of 95 ± 22 and 52 ± 18 nm, and mean widths of 16 ± 4 and 9 ± 3 nm, respectively, in the transverse slice for each species. These species present regions with nanocrystalline sizes reaching up to 147 nm in length and 26 nm in width for *H. horridum* and 97 nm in length and 15 nm in width for *B. major*. Together with this impressive nanocrystalline size, both species present an extremely low degree of crystallographic texture, as shown in **Figure** 7b,f. These large crystallites are arranged nearly isotropically within the ≈20 µm domain size probed by the scanning X-ray diffraction experiment. On the other hand, the capping tissue of the *P. apodus*, *C. zebrata*, *T. scincoides*, and *T. rugosa* displays smaller crystallites than those in bone. The mean sizes for these species stay between 22 ± 2 and 25 ± 1 nm in length and 3.4 ± 0.2 and 5.2 ± 0.2 nm in width, with the smallest and largest crystallites belonging to the *P. apodus* and *C. zebrata*, respectively. The complete list of mean crystallite sizes can be found in the Table S6 (Supporting Information). Surprisingly, these smaller crystallite sizes present a higher degree of crystallographic texture than the surrounding bone (Figure 7f), with the special mention of the crystallites of *P. apodus* in Figure 7a, which have a considerably higher degree of texture than all other species. Overall, the crystallite sizes in capping tissue appear much more uniform than previously

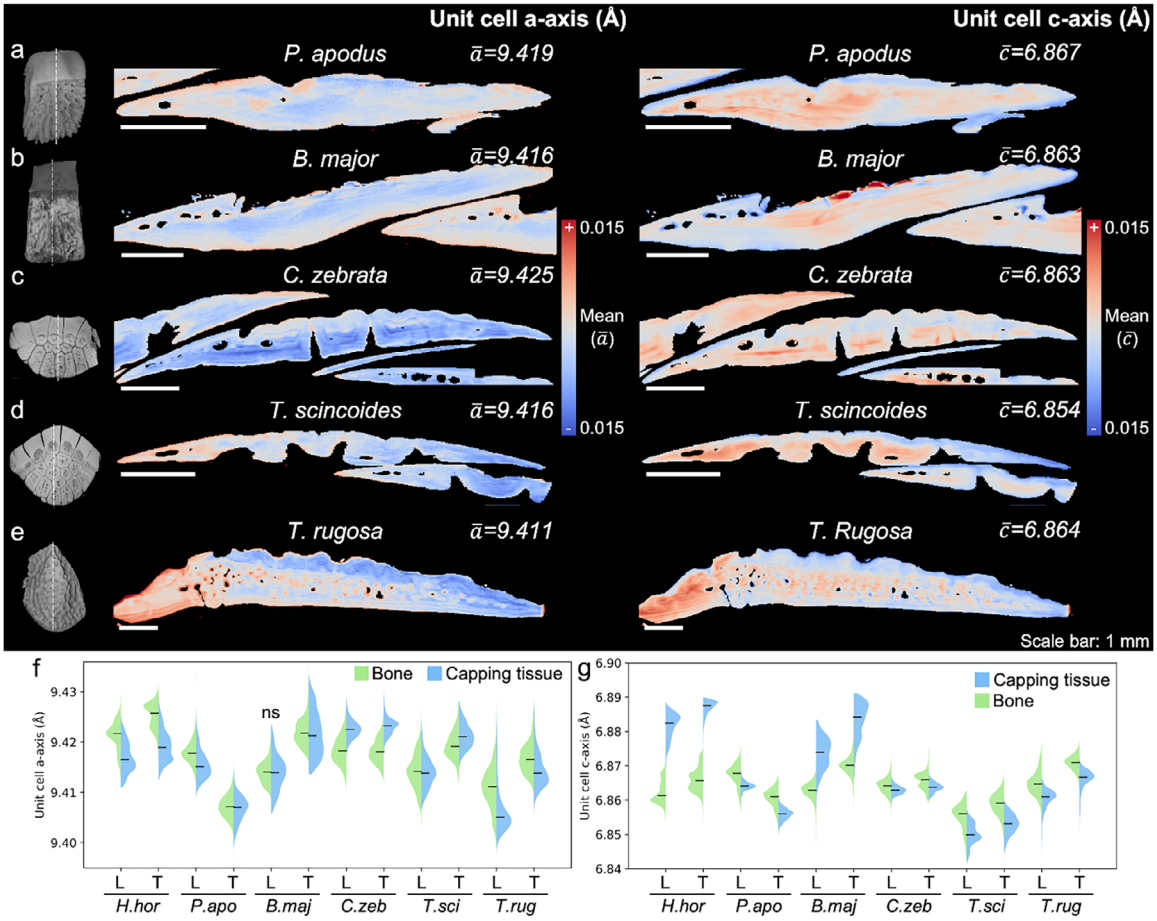

Figure 5. Deviations from the crystallographic unit cell parameter maps of osteoderm longitudinal slices. 3D renderings and Rietveld refined X-ray diffraction scanning maps expressed as the +/− 0.015 Å from the mean value for (a) *Pseudopus apodus*, b) *Broadleysaurus major*, c) *Corucia zebrata*, d) *Tiliqua scincoides*, and e) *Tiliqua rugosa*. f,g) Violin plots summarizing the unit cell (f) *a*-axis and (g) *c*-axis in the capping tissue and bone in the longitudinal (*L*) and transverse (*T*) slices for the species of interest, with mean values in Table S5 (Supporting Information). All bone-capping tissue comparisons within each measurement show statistical significance, $p < 0.001$, unless specified "ns" (see Tables S11 and S12, Supporting Information). The approximate location of the thin slice is shown on the 3D renderings in dashed lines. Note that the osteoderm slices were not obtained from the same osteoderm displayed on the left-side panel. Additional scanning maps on the transverse cross-section can be found in Figure S9 (Supporting Information).

reported size maps in the *H. horridum* for both capping tissue and bone.

To seek trends in structural and mechanical properties, we compare these in bivariate plots inspired by Ashby plots[50] in **Figure 8**. In most cases, *H. horridum* and *B. major* stand out. The *a* and *c* lattice parameters (Figure 8a) form groupings differentiated mostly by the *c*-axis as described above. The crystal sizes parallel and perpendicular to the *c*-axis follow an overall linear trend (Figure 8b), indicating that the increasing crystallite size in one dimension generally is accompanied by an overall growth in crystal volume. The striking division of capping tissue between species stands out clearly here, with *H. horridum* and *B. major* on one side of the bone values, while all other species group on the other. This division into two groups is particularly interesting since they also showed different staining properties in previous histological studies: *H. horridum* and *B. major* did not show any apparent staining in the capping tissue, while *P. apodus*, *C. zebrata*, *T. scincoides*, and *T. rugosa* capping tissue appeared as basophilic tissue.[23,36] The large degree of mineralization of most capping tissues does not necessarily correlate with the nanostructure of the mineral, as species with a high degree of mineralization present both larger and smaller unit cell *c*-axis (Figure 8d) and a wide range of crystallite sizes (Figure 8e). However, the high degree of mineralization does relate to the mechanical performance of the capping tissue, with a higher elastic modulus for species with higher mineral content (Figure 8f). Focusing on the nanostructure of such crystallites, which seems to be a factor dividing species into two groups, the crystallite size strongly correlates with the length of the unit cell axes (Figure 8g) and crystallographic texture index (Figure 8h), indicating a possible determining factor in the mineralization process and categorization of such processes. Surprisingly, larger crystallites do not appear together with high mechanical performance (Figure 8i), as high nanoindentation stiffness and hardness are achieved both by large unoriented and by small, oriented hydroxyapatite elongated nanocrystals.

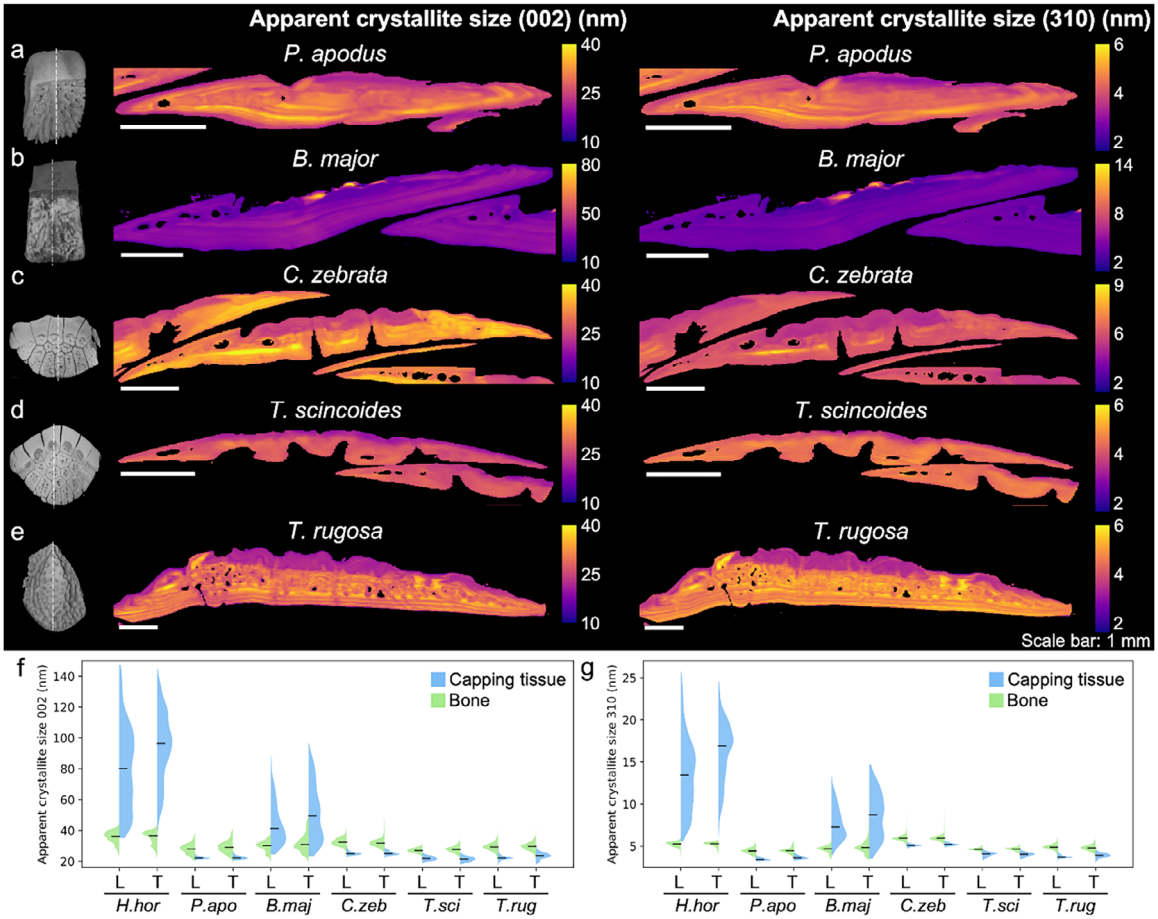

Figure 6. Apparent crystallite length and width maps of osteoderm longitudinal slices. 3D renderings and hydroxyapatite crystallite size in the 002 (length) and 310 (width) crystallographic directions obtained from the X-ray diffraction scanning maps for (a) *Pseudopus apodus*, b) *Broadleysaurus major*, c) *Corucia zebrata*, d) *Tiliqua scincoides*, and e) *Tiliqua rugosa*. Note that the color scales vary between subfigures for visibility. f,g) Violin plots summarizing the crystallite size (f) parallel and (g) perpendicular to the lattice *c*-axis in the capping tissue and bone in the longitudinal (*L*) and transverse (*T*) slices for the species of interest, with mean values in Table S6 (Supporting Information). All bone-capping tissue comparisons within each measurement show statistically significant differences between bone and capping tissue, $p < 0.001$ (see Tables S13 and S14, Supporting Information). The approximate location of the thin slice is shown on the 3D renderings in dashed lines. Note that the osteoderm slices were not obtained from the same osteoderm displayed on the left-side panel. Additional scanning maps on the transverse cross-section can be found in Figure S10 (Supporting Information).

To summarize, two species feature capping tissue with larger crystallites arranged with a very low degree of texture, while the other four species, in stark contrast to the first group, present crystallites smaller than in bone but with a higher degree of texture. This demonstrates a remarkable structural diversity in capping tissues. This diversity might be speculated to be related to the biological function of the capping tissue in each species. However, the differences in capping tissue biological functions remain an area of active research. There is a consensus emerging that while a defensive function seems to dominate, diverse secondary functions are likely to be very important.[17,23] However, no general pattern has emerged as of yet to relations between osteoderm function and for example, phylogeny, geography, and/or ecology. Thus, we conclude that more research is needed on the relationship between osteoderm structure and its biological function.

2.4. Influence of the Capping Tissue-Bone Interface on the Mechanical Properties

To help understand the mechanical relevance of the observed nanostructure variation across the different species, we constructed idealized and simplified osteoderm finite element models. Two primary investigations were carried out related to 1) the effect of the transition zone thickness between the capping and bone tissues and 2) the level of anisotropy in the capping tissue, modeling the observed variation in the degree of texture. These parameters were observed to vary greatly across species. We restrict ourselves to exploring these parameters because the model is purposely made simple so as to avoid complications from variations in microstructure, e.g., pores, etc., within the osteoderms.

As expected,[51] the increased thickness of the transition zone resulted in a clear reduction in stress concentration (**Figure 9b**)

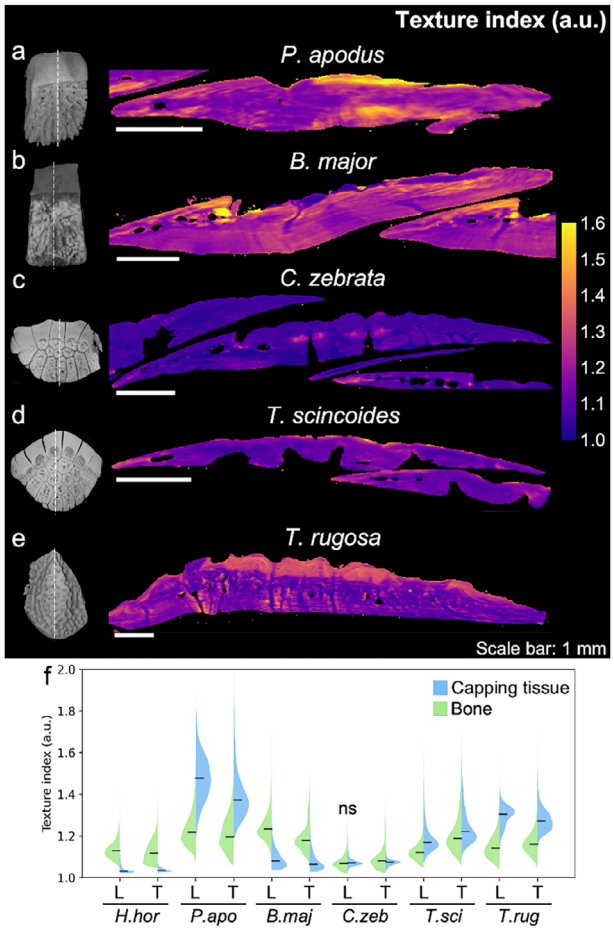

Figure 7. Crystallographic degree of texture maps of osteoderm longitudinal slices. 3D renderings and hydroxyapatite texture index obtained from the X-ray diffraction scanning maps for (a) *Pseudopus apodus*, b) *Broadleysaurus major*, c) *Corucia zebrata*, d) *Tiliqua scincoides*, and e) *Tiliqua rugosa*. Note that the color scales vary between subfigures for visibility. f) Violin plots summarizing the texture index in the capping tissue and bone in the longitudinal (*L*) and transverse (*T*) slices for the species of interest, with mean values in Table S7 (Supporting Information). All bone-capping tissue comparisons within each measurement show statistical significance, $p < 0.001$, unless specified "ns" (see Table S15, Supporting Information). Note that the osteoderm slices were not obtained from the same osteoderm displayed on the left-side panel. Additional maps on the transverse cross-section can be found in Figure S11 (Supporting Information).

in the boundary region. The maximum von Mises stress reduced with increased transition depth from 130, 122, and 98 MPa (capping tissue, transition zone, and bone) at 0.002 mm transition thickness (no gradient condition) to 61, 78, and 55 MPa (capping tissue, transition zone, and bone) at 0.498 mm transition zone thickness (full capping tissue gradient condition). Even a marginal increase in transition depth from 0.002 to 0.1 mm gradient thickness resulted in ≈25% decrease in maximum stress across the three regions. These results highlight the significant impact of transition gradient thickness on stress concentration, with a reduction in stress concentration with an increased gradient region. Specifically, it may highlight the functional implications of the observed transition zone in *H. horridum* and *P. apodus*. However, functionally, it may be more important in *H. horridum* as the level of stress concentration is higher in this case, where the stiffness of the capping tissue is significantly higher than the bone stiffness. Thus, the relative importance of the gradient in *P. apodus* for stress concentration mitigation is likely smaller as the stress concentration is expected to be significantly lower than in *H. horridum*.

The level of anisotropy contributes less to the response than the gradient thickness. Comparison of the fully isotropic case to the fully longitudinally aligned anisotropic case in Figure 9e,f highlights small differences between the two cases. Some differences are observed, primarily lower strain values across the capping tissue region and lower stress values in the capping and transition zone, with no apparent change to the distribution patterns. The changes in maximum strain represent a 12% decrease in capping tissue and <1% change across both transition and bone regions. Regarding maximum stress, 8%, 6% decreases, and 3% increase were observed in capping, transition, and bone regions, respectively. Thus, increased crystallographic texture may contribute to improved transfer of stress even if the effect is small.

Here, the investigations for both transition thickness and level of capping tissue anisotropy were carried out assuming isotropic bone properties. When considering anisotropic bone properties regardless of the anisotropic alignment (longitudinal or transverse to the loading axis), the effects of transition depth and level of capping tissue anisotropy appear to remain consistent (see Figure S14, Supporting Information). This may, however, change when also including microstructure effects such as pores.

To determine whether the modelling of the capping tissue meaningfully affects the response of the simplified osteoderm model to external loading, the capping tissue material properties were varied. The properties were linearly interpolated from the anisotropic capping tissue properties to the bone material properties, in effect resulting in a full bone osteoderm model. Figure S16a,b (Supporting Information) highlights the differences between the two extremes. Regarding the strain contour, the strain appears to be distributed throughout the structure in the full bone osteoderm, while inclusion of the capping region limits the deformation to the bone region. However, as the relative material properties of the capping tissue increase, the stress concentrates in the transition zone. Inclusion of the capping tissues results in ≈24% reduction in average strain across all regions (Figure S16e, Supporting Information), accompanied by a ≈14% increase in average stress (Figure S16f, Supporting Information). However, due to the stress concentration, the maximum stress increased by ≈60% from 60 to 99 MPa.

The finite element model included a similar ratio of the capping tissue to bone material properties as in the nanoindentation results for *H. horridum*. This suggests that stress concentration during loading will be the highest in *H. horridum* osteoderms compared to the other species. This highlights that the nanostructure of these osteoderms may limit deformation via the stiff capping tissue while at the same time minimizing the resulting stress concentration through the inclusion of a transition zone between the capping tissue and bone. We note that the present modeling does not take anchoring within the tissue through, for example, Sharpey's fibers into account. The stress transfer to soft tissue can be expected to play an important role in overall tissue

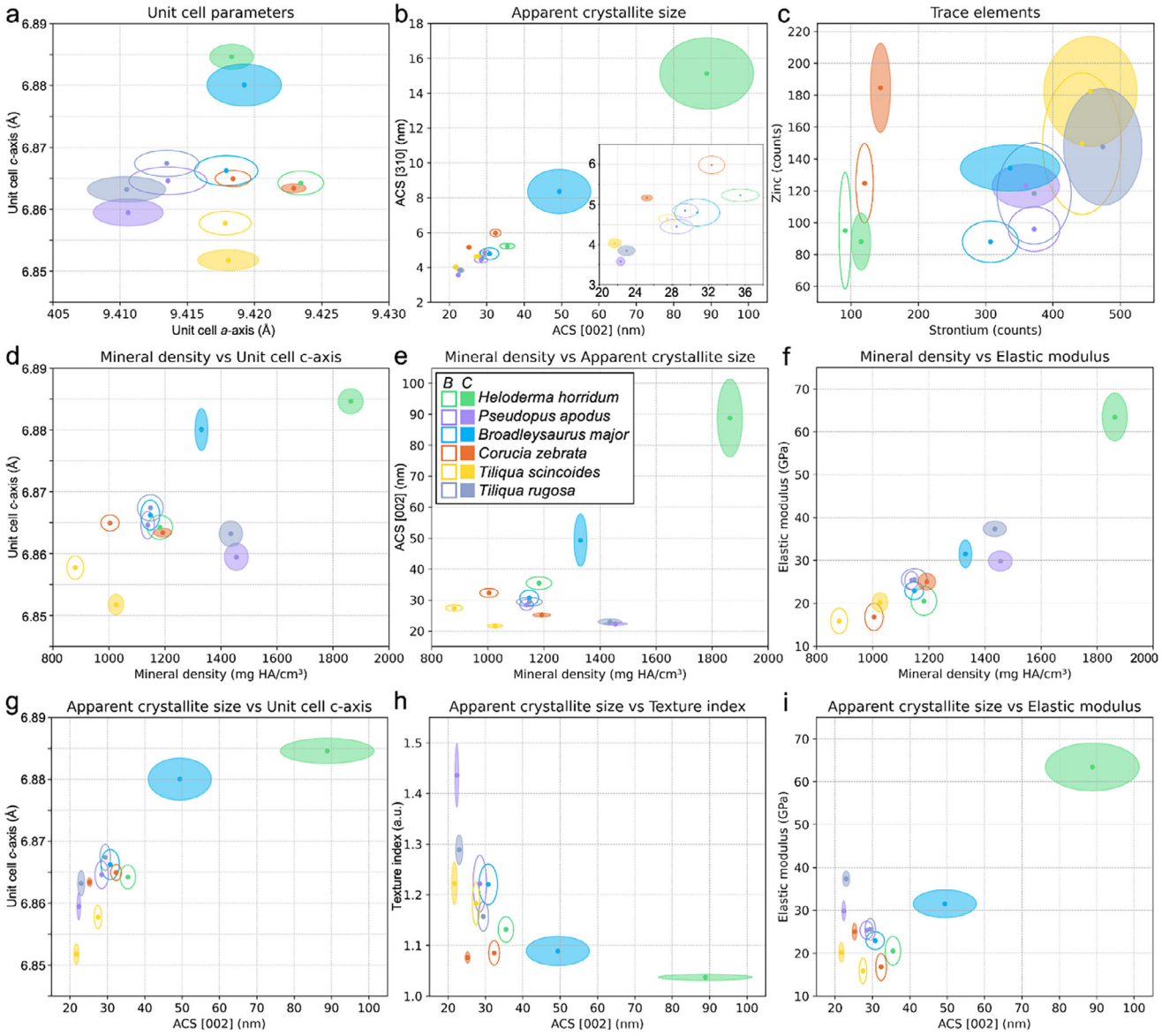

Figure 8. Summary of parameters for all species. Ashby plots with the mean (symbol) and standard deviation (ellipse) of each species in the study. Bone (*B*, open symbols) and capping tissue (*C*, closed symbols) are shown.

biomechanics, but it is beyond the scope of the present work. Building on the nanostructure characterization presented here, future whole-head lizard finite element models[52] augmented by the capping/bone tissue modelling may help understand the nanostructure effects on the skull mechanics.

3. Conclusion

In this work, we used a combination of techniques to provide the first comparative investigation of osteoderm capping tissue nanostructure across a diverse set of lizard species. To the best of our knowledge, this represents a singular effort at comprehensive cross-species comparison of the same tissue type for tissues other than bone. Capping tissue, located on the dorsal side of the osteoderm, is consistently more mineralized and generally stiffer and harder than the underlying bone. However, its degree of mineralization, morphology, mechanical performance, and nanostructure strikingly vary among taxa. In all species examined, the capping tissue is composed of hydroxyapatite and enriched in strontium and/or zinc relative to bone, even if the spatial distribution of these elements differs considerably. While the capping tissue is universally stiffer and harder than osteoderm bone, the degree of stiffening ranges widely, from values only slightly above those of bone to some of the highest reported for reptilian skeletal tissues.

At the nanostructural level, two major groups emerge: one represented by *Heloderma horridum* and *Broadleysaurus major*, with unusually large, nearly isotropic crystals and very high stiffness, and another encompassing *Pseudopus apodus*, *Corucia zebrata*, *Tiliqua scincoides*, and *Tiliqua rugosa*, where the capping tissue

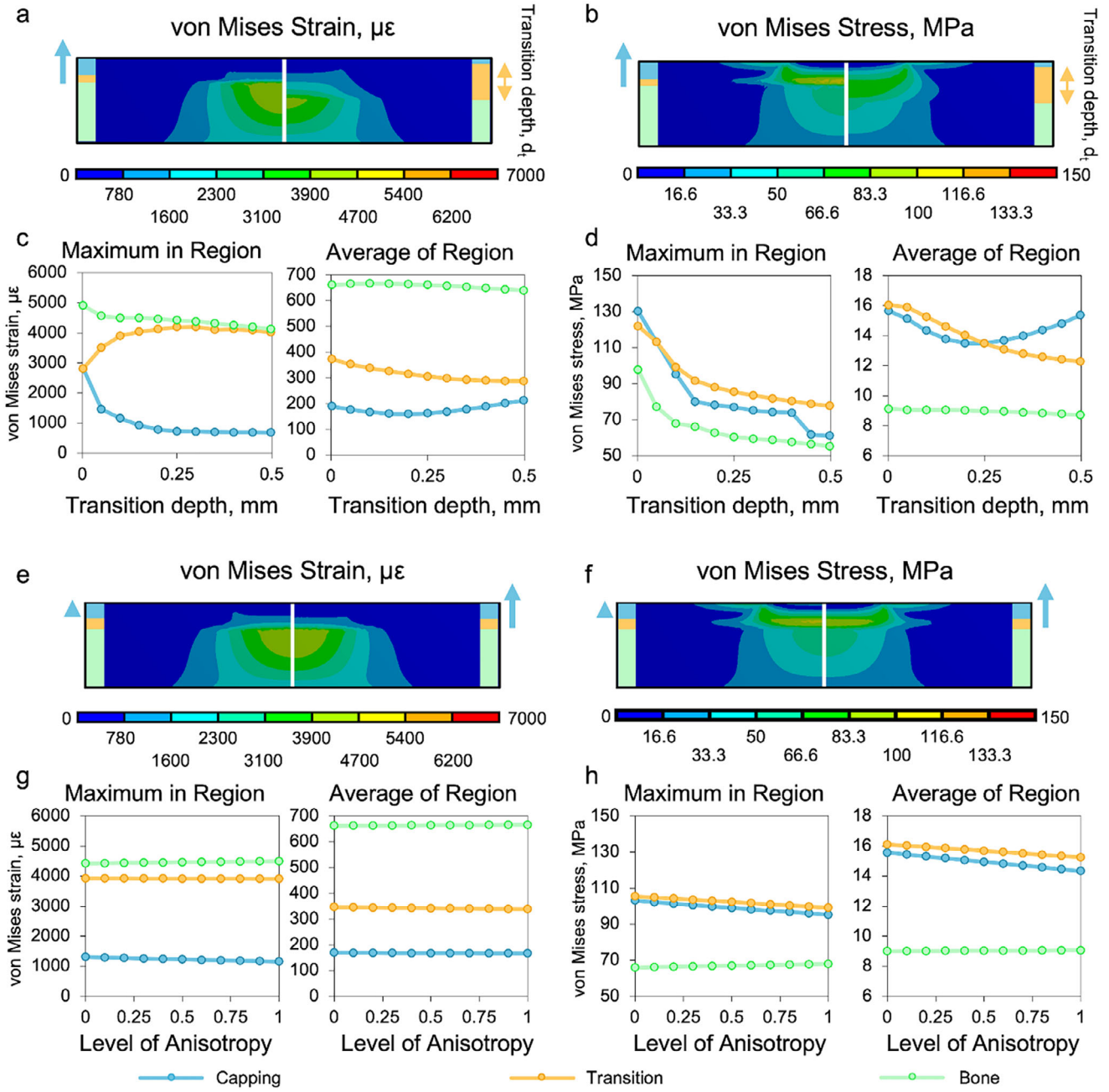

Figure 9. Effect of transition zone thickness and capping tissue texture in a simplified osteoderm finite element model. a–d) Effect of transition thickness variation from 0.002 to 0.498 mm, (a) contour plot of the von Mises strain in 0.05 mm (left) and 0.45 mm (right) transition cases, (b) contour plot of the von Mises stress (MPa) in 0.05 mm (left) and 0.45 mm (right) transition cases, (c) maximum and average von Mises strain in each region against transition depth, (d) maximum and average von Mises stress (MPa) in each region against transition depth. e,f) Effect of level of anisotropy in the capping tissue aligned longitudinally with the load, (e) contour plot of the von Mises strain in 0% (left) and 100% (right) longitudinally anisotropic cases, (f) contour plot of the von Mises stress (MPa) in 0% (left) and 100% (right) longitudinally anisotropic cases, g) maximum and average von Mises strain in each region against transition depth, h) maximum and average von Mises stress (MPa) in each region against transition depth. Results for the same analyses with anisotropic bone properties are available in Figure S15 (Supporting Information).

is characterized by smaller, more textured crystals and mechanical properties closer to bone. The correlation between crystal size and unit cell parameters further underscores the importance of fine-scale mineral organization in driving tissue performance. Together, these findings demonstrate that capping tissue represents a highly variable but functionally important specialization in lizard osteoderms, likely shaped by a combination of phylogenetic and ecological factors.

The present results suggest that a high degree of mineralization, by itself, does not guarantee excellent mechanical

Table 1. Summary of samples and techniques used for all of the species measured.

Individual number	Osteoderm label	X-ray computed tomography	Nanoindentation	Scanning X-ray diffraction	Scanning X-ray fluorescence
1	A	X			
1	B			X	X
1	C			X	X
1	D		X		
2	A		X		

performance. Rather, a more complex interplay of crystallite size and spatial arrangement seems to determine performance. The two classes of capping tissues display much lower and much higher degrees of texture than the underlying bone, suggesting that diverse structural organizations may have evolved, likely independently, to afford the highly mineralized osteoderm capping tissues.

4. Experimental Section

Sample Preparation: Osteoderms of a total of six different species of lizards were used in this study. The lizard specimens were taken from Anthony Herrel's collection and from those supplied for research from the National Museum of Natural History (France). The osteoderms with dermis and epidermis (See Figure S1, Supporting Information) were obtained from the dorsal cervical midline of adult male/female *Pseudopus apodus* (Collection ID Herrel: PA1,2), *Broadleysaurus major* (Collection ID Herrel: BM1,2), *Corucia zebrata* (Collection ID Herrel: CZ1,2), *Tiliqua scincoides* (Collection ID Herrel: TS1,2), and *Tiliqua rugosa* (Collection ID Herrel: TR1,2). Additionally, the published X-ray imaging dataset on osteoderms from *Heloderma horridum*[26,53] was accessed for the final comparison between species. The samples were fixed by placing the tissue in 10% aqueous formaldehyde for 48 h, after which it was rinsed and transferred to 70% ethanol for storage.

A total of five osteoderms per species were used in this study, with four belonging to the same individual (**Table 1**). One osteoderm, suspended in 70% ethanol-infused agar gel, was used for X-ray computed tomography. Two osteoderms were embedded in EpoFix resin (Struers ApS, Denmark) and sequentially sliced in the transverse and sagittal planes, respectively, using a diamond-blade saw (Accutom-5, M1D15 wheel, Struers ApS, DK) with a final thickness of 130–185 µm. The thin slices were placed on Kapton tape and mounted on metallic rectangular frames for scanning X-ray diffraction (XRD) and X-ray fluorescence spectroscopy (XRF). Finally, two osteoderms from different individuals were similarly embedded in EpoFix resin and halved in the sagittal plane with the diamond-blade saw for nanoindentation. The inner surface of the osteoderms was then prepared by polishing with silicon carbide paper (800, 1200, 2400 grit) and a diamond suspension with a final roughness of ≈1 µm.

X-Ray Microscopy and Computed Tomography: X-ray computed tomography was performed in a Versa 620 X-ray microscope (ZEISS, Germany). A conical X-ray beam was produced using an accelerating voltage of 60 kVp and a power of 6.5 W and filtered using a low-energy filter. A total of 3201 X-ray projections in the range 0–360° were collected on a CCD camera coupled to a 0.4 × magnification objective equipped with a scintillator. The tomographic reconstructions were conducted using the TXM Reconstructor Scout-and-Scan software provided with the instrument (ZEISS, Germany) using a cone beam adapted filtered back projection (FBP) algorithm, resulting in an isotropic voxel size given in **Table 2**. The tomographic slices were processed and analyzed using the software Dragonfly (Comet Technologies Canada Inc.).

For quantitative analyses, micro X-ray computed tomography using calibrated gray-value intensities was performed on a subsection of the osteoderms using a Scanco µCT35 desktop micro-CT system (SCANCO, Switzerland). Scanning was conducted at an acceleration voltage of 55 kVp for all the species except *H. horridum*, for which 70 kVp was used, and a power of 8 W, with an isotropic voxel size of 3.5 µm. A total of 1000 projections over 180° were acquired with an integration time of 800 ms. An aluminum filter was applied to prevent beam hardening effects. Quantification of bone and capping tissue mineral density was done by applying a Gaussian filter to the reconstructed slices ($\sigma = 2$) for noise reduction and fitting a triple Gaussian to the histograms.

X-ray transmission radiographies were measured in the Versa 620 X-ray microscope (ZEISS, Germany) on the slices used for scanning XRD and XRF. The X-ray transmission images were obtained by averaging 10 radiographies collected with a 5 s exposure time each. Flat-field correction was applied to the images using 10 images and 5 s exposure time for each (See Figures S3 and S4, Supporting Information).

Scanning X-Ray Diffraction and Fluorescence Spectroscopy: Simultaneous scanning X-ray diffraction (XRD) and X-ray fluorescence (XRF) measurements were performed at the DanMAX beamline of the MAX IV laboratory synchrotron (Sweden). A monochromatic X-ray beam with an energy of 17.00 keV was obtained with a Si(111) double-crystal monochromator and focused to 43.9 × 15.0 µm in the horizontal and vertical directions (full-width half maximum), using a compound refractive lens transfocator. A motorized stage with 2-axis movement in the plane perpendicular to the beam was used to raster scan the osteoderm slices with fly-scanning movement in the vertical direction at a scanning rate of 80 Hz (12.5 ms per point) in steps of 20 × 10 µm in the horizontal and vertical directions, respectively. The diffraction signal was recorded at each scanning point by a PILATUS3 X 2 M CdTe detector[54] (Dectris, Switzerland) in transmission geometry at a sample-to-detector distance of 0.2350 m. A tungsten beam stop was placed between the sample and the detector to block the direct beam. The tungsten beam stop had an internal aluminum wire to stop fluorescence from the Tungsten *L* edge. The X-ray fluorescence signal from the sample was measured by a SiriusSD detector (RaySpec Ltd., UK) at a sample-to-detector distance of 175 mm and turned 36° in relation to the incident beam. To account for possible texture artefacts, two perpendicular osteoderm slices (transverse and longitudinal) were measured.

The X-ray diffraction signal was radially integrated to a *q*-range of 1.5–41.6 nm^{-1} using the software MatFRAIA.[55] The integrated diffraction data were Rietveld refined using a hydroxyapatite model in the range *q*

Table 2. X-ray computed tomography parameters.

Species	Acquisition time [s]	Voxel size [µm]
Heloderma horridum	12	1.498
Pseudopus apodus	10	3.815
Broadleysaurus major	15	4.498
Corucia zebrata	6	5.488
Tiliqua scincoides	7	5.821
Tiliqua rugosa	5	5.503

= 16.64–39.96 nm^{-1} with the software MultiRef[49] and GSAS.[56] The model used consisted of a background function (10-coefficient Chebyshev polynomial expansion), lattice constants, scale factor, profile parameters describing an anisotropic size broadening model, as well as a spherical harmonics description of preferred orientation. The obtained refinement results were combined into the corresponding 2D images, excluding points where convergence was not achieved (these were points without any diffraction signal). A final intensity mask was applied to remove the area outside the osteoderm.

The XRF data were processed and fitted using the software PyMCA[57] to map variations in elemental composition across the osteoderm and masked in the same manner as the XRD results.

Nanoindentation: Nanoindentation measurements were performed using a Hysitron TriboIndenter (Hysitron, Minneapolis, MN) with a Berkovich tip. Nanoindentation maps were obtained by measuring multiple indentations using a maximum load of 1000 µN and a distance between indents of 10 µm. A 10 s load, 30 s stabilization time, and 10 s unload scheme was used to ensure relaxation of viscoelastic effects. The unloading segment in each indent was fitted, and the reduced elastic modulus (*Er*) and hardness (*H*) were calculated using the Oliver–Pharr method.[58]

Finite-Element Mechanical Simulation: An idealized, simplified, and parameterized osteoderm model was developed in Ansys Workbench (ANSYS Inc., Canonsburg, PA, USA). Figure S12a (Supporting Information) shows the base model loosely based on the investigated osteoderms. A 2.5 mm radius cylinder with a 1 mm height was chosen to represent an osteoderm. Height-based regions were defined to represent the capping tissue (1–0.8 mm), transition zone (0.8–0.7 mm), and bone region (0.7–0 mm). Material properties across the transition zone were linearly interpolated with respect to the height coordinate, where at the lower limit of the region, the material properties were bone, while at the higher limit, the properties were capping tissue.

Regarding the boundary conditions, the full bottom surface was displacement-constrained in all directions. A 0.75 mm radius centered disc on the top surface was subjected to a 150 N compressive force in the Z direction. The sides were not constrained.

This simplified model was chosen for two main reasons. First, due to the extreme variation in both morphology and nanostructure between species, it is unclear what a more specific representative model would be. Second, the analyses were carried out to understand the mechanical effects of the observed nanostructure in general, rather than in the specific species. However, future work could include finite element (FE) modelling of species-specific geometry and nanostructure/material properties.

All investigations recorded von Mises, 1st and 3rd principal maximum and average strains and stresses in the full osteoderm and the three individual regions (capping tissue, transition, and bone) as well. Additionally, cross-sectional (XZ plane) contour plots were produced for the von Mises stress and strain results.

The material properties obtained from the nanoindentation in this work were not used in the finite element analyses, as critically, the finite element analyses focus on the anisotropic capping tissue properties. Thus, the material properties used are presented in Table S17 (Supporting Information) with the anisotropic values obtained from literature for hydroxyapatite for capping tissue[59] and cortical bone for the bone region.[60] Two primary analyses were carried out and included in the main text. These investigated the transition depth effects, where the thickness of the transition zone was varied from 0.002 mm depth to 0.498 mm centered at 0.75 mm height, and the level of anisotropy in the capping tissue, where the capping tissue material properties were linearly interpolated between the isotropic and anisotropic properties (as shown in Figure S13b, Supporting Information) available in Table S17 (Supporting Information), on the mechanical response of the model. Additionally, further sensitivity analyses were carried out, including mesh convergence (as shown in Figure S13a, Supporting Information) in Figure S14a (Supporting Information). Across all other investigations, the model consisted of 1355033 tetrahedral elements

Statistical Analysis: Quantification and statistical analysis of the measured data were performed using masks for the regions containing the capping tissue and bone. The masks in the nanoindentation maps were obtained by visual identification of the regions of interest in optical microscopy images. The segmentation of the XRD and XRF scanning maps was carried out with X-ray radiographies of the measured slices. The capping tissue was identified by the higher absorption contrast in the radiographies, coinciding with the higher mineral density in the tissue (see Figures S3 and S4, Supporting Information). Mean values with standard deviation for all parameters presented in this study can be found in Tables S1–S6 (Supporting Information).

Statistics were performed in R (version 4.3.1) using packages dplyr, emmeans, glmmTMB, purrr. performance visualized individually in DHARMa. For XRF and XRD data, a generalized linear model was constructed within each species with *Sample* (i.e., osteoderm thin slice) and *Tissue* (segmented capping tissue vs bone) as fixed effects (given that there were two samples per species – both from the same individual) with *Tissue* nested within *Sample*. A gamma log link structure was used to account for data shape, and contrasts were performed at the level of tissue on the response scale. *p*-values were adjusted for multiple comparisons (Holm Bonferroni correction), and are presented only as a reference due to the fine scale of the data considered. For nanoindentation data, a similar model within species was constructed to compare capping tissue and bone, with individual and sample as nested fixed effects, due to the low number of levels of both, and averaging over the levels of grid (representing osteodermite). Values for the model estimate with standard deviation and *p*-values for the bone-capping tissue comparisons are shown in the Tables S7–S15 (Supporting Information).

Supporting Information

Supporting Information is available from the Wiley Online Library or from the author.

Acknowledgements

The authors acknowledge the MAX IV Laboratory for time on Beamline DanMAX under proposal 20230245. Research conducted at MAX IV was supported by the Swedish Research Council under contract 2018-07152, the Swedish Governmental Agency for Innovation Systems under contract 2018-04969, and Formas under contract 2019-02496. DanMAX was funded by the NUFI grant no. 4059-00009B. The XRF detector was made available by Aarhus University through grant CF18-0802 from the Carlsberg Foundation. The authors thank the Danish Agency for Science, Technology, and Innovation for funding the instrument center DanScatt. The use of the Novo Nordisk Foundation research infrastructure AXIA (grant NNF19OC0055801) is gratefully acknowledged. Support from Nordforsk (grant number 105053) is gratefully acknowledged. Samples were made available via the HSFP-funded project Human Frontier Science Program (RGP0039/2019). ARP has received funding from the European Union's Horizon 2020 research and innovation program under the Marie Skłodowska-Curie grant agreement No 101152202. Support from the Novo Nordisk Foundation (XTREME-CT, grant NNF22OC0077698) is gratefully acknowledged. The VELUX Foundation is acknowledged for donating the desktop micro-CT system.

Conflict of Interest

The authors declare no conflict of interest.

Author Contributions

A.R.-P. did conceptualization, methodology, investigation, data curation, formal analysis, visualization, writing of the original draft, and writing of the review & editing. M.D. did investigation, writing of the original draft, and writing of the review & editing. M.S.B.J., T.E.K.C., I.K., M.R.V.J., and

K.P.A. did investigation and writing of the review & editing. A.H. did resources and writing of the review & editing. J.S.T. did investigation and writing of the review & editing. C.W. did conceptualization, methodology, investigation, formal analysis, writing of the original draft, and writing of the review & editing. H.B. did conceptualization, methodology, investigation, formal analysis, funding acquisition, writing of the original draft, and writing of the review & editing.

Data Availability Statement

The data that support the findings of this study are openly available in Zenodo at https://doi.org/10.5281/zenodo.16361662, reference number 16361662.

Keywords

biomineralization, diffraction, lizard osteoderm, mechanics, X-ray imaging

Received: September 30, 2025
Revised: October 31, 2025
Published online:

[1] A. Rodriguez-Palomo, M. Østergaard, H. Birkedal, *Adv. Funct. Mater.* **2023**, *34*, 2307026.
[2] N. K. Wittig, H. Birkedal, *Acta Cryst.* **2022**, *78*, 305.
[3] N. Reznikov, M. Bilton, L. Lari, M. M. Stevens, R. Kröger, *Science* **2018**, *360*, aao2189.
[4] D. J. Buss, R. Kröger, M. D. McKee, N. Reznikov, *J. Struct. Biol.: X* **2022**, *6*, 100057.
[5] T. A. Grünewald, M. Liebi, N. K. Wittig, A. Johannes, T. Sikjaer, L. Rejnmark, Z. Gao, M. Rosenthal, M. Guizar-Sicairos, H. Birkedal, M. Burghammer, *Sci. Adv.* **2020**, *6*, aba4171.
[6] M. Al-Jawad, A. Steuwer, S. H. Kilcoyne, R. C. Shore, R. Cywinski, D. J. Wood, *Biomaterials* **2007**, *28*, 2908.
[7] C. A. Stifler, J. E. Jakes, J. D. North, D. R. Green, J. C. Weaver, P. U. P. A. Gilbert, *Acta Biomater.* **2021**, *120*, 124.
[8] L. M. Simmons, M. Al-Jawad, S. H. Kilcoyne, D. J. Wood, *Eur. J. Oral Sci.* **2011**, *119*, 19.
[9] M. A. Marcus, S. Amini, C. A. Stifler, C.-Y. Sun, N. Tamura, H. A. Bechtel, D. Y. Parkinson, H. S. Barnard, X. X. X. Zhang, J. Q. I. Chua, A. Miserez, P. U. P. A. Gilbert, *ACS Nano* **2017**, *11*, 11856.
[10] S. Bentov, P. Zaslansky, A. Al-Sawalmih, A. Masic, P. Fratzl, A. Sagi, A. Berman, B. Aichmayer, *Nat. Commun.* **2012**, *3*, 839.
[11] W. Yang, B. Gludovatz, E. A. Zimmermann, H. A. Bale, R. O. Ritchie, M. A. Meyers, *Acta Biomater.* **2013**, *9*, 5876.
[12] H. Quan, W. Yang, E. Schaible, R. O. Ritchie, M. A. Meyers, *Adv. Funct. Mater.* **2018**, *28*, 1804237.
[13] B. J. F. Bruet, J. Song, M. C. Boyce, C. Ortiz, *Nat. Mater.* **2008**, *7*, 748.
[14] P. G. Allison, M. Q. Chandler, R. I. Rodriguez, B. A. Williams, R. D. Moser, C. A. Weiss, A. R. Poda, B. J. Lafferty, A. J. Kennedy, J. M. Seiter, W. D. Hodo, R. F. Cook, *Acta Biomater.* **2013**, *9*, 5289.
[15] W. Yang, I. H. Chen, B. Gludovatz, E. A. Zimmermann, R. O. Ritchie, M. A. Meyers, *Adv. Mater.* **2013**, *25*, 31.
[16] R. Ebel, C. Broeckhoven, E. L. Stanley, T. Ramm, J. S. Keogh, *Zool. J. Linnean Soc.* **2025**, *204*, zlaf070.
[17] C. Williams, A. Kirby, A. Marghoub, L. Kéver, S. Ostashevskaya-Gohstand, S. Bertazzo, M. Moazen, A. Abzhanov, A. Herrel, S. E. Evans, M. Vickaryous, *Biol. Rev.* **2022**, *97*, 1.
[18] A. Maliuk, A. Marghoub, C. J. A. Williams, E. Stanley, L. Kéver, M. Vickaryous, A. Herrel, S. E. Evans, M. Moazen, *Anat. Rec.* **2024**, *307*, 3191.
[19] M. Maden, T. Polvadore, A. Polanco, W. B. Barbazuk, E. Stanley, *iScience* **2023**, *26*, 106779.
[20] P. Frýdlová, V. Janovská, J. Mrzílková, M. Halašková, M. Riegerová, J. Dudák, V. Tymlová, J. Žemlička, P. Zach, D. Frynta, *Sci. Rep.* **2023**, *13*, 6405.
[21] V. de Buffrénil, Y. Dauphin, J.-C. Rage, J.-Y. Sire, *Comptes Rendus Palevol* **2011**, *10*, 427.
[22] F. Iacoviello, A. C. Kirby, Y. Javanmardi, E. Moeendarbary, M. Shabanli, E. Tsolaki, A. C. Sharp, M. J. Hayes, K. Keevend, J.-H. Li, D. J. L. Brett, P. R. Shearing, A. Olivo, I. K. Herrmann, S. E. Evans, M. Moazen, S. Bertazzo, *Acta Biomater.* **2020**, *107*, 194.
[23] G. Willan, Master of Science MSc Thesis, University of Guelph, Guelph, ON, Canada, **2024**.
[24] A. Marghoub, C. J. A. Williams, J. V. Leite, A. C. Kirby, L. Kéver, L. B. Porro, P. M. Barrett, S. Bertazzo, A. Abzhanov, M. Vickaryous, A. Herrel, S. E. Evans, M. Moazen, *Acta Biomater.* **2022**, *146*, 306.
[25] L. Kéver, D. Olivier, A. Marghoub, S. E. Evans, M. K. Vickaryous, M. Moazen, A. Herrel, *J. Exp. Biol.* **2022**, *225*, jeb244551.
[26] A. Rodriguez-Palomo, M. S. B. Jacobsen, T. E. K. Christensen, M. R. V. Jørgensen, I. Kantor, G. Willan, A. Herrel, A. Marghoub, M. Moazen, S. Evans, M. Vickaryous, C. J. A. Williams, H. Birkedal, *Acta Biomater.* **2025**, *204*, 457.
[27] E. Beniash, C. A. Stifler, C.-Y. Sun, G. S. Jung, Z. Qin, M. J. Buehler, P. U. P. A. Gilbert, *Nat. Commun.* **2019**, *10*, 4383.
[28] H. Dominguez-Vega, D. Beck, in *The IUCN Red List of Threatened Species*, International Union for Conservation of Nature, Gland, Switzerland **2021**.
[29] A. Aghasyan, A. Avci, B. Tuniyev, J. Crnobrnja-Isailovic, P. Lymberakis, C. Andrén, D. Cogalniceanu, J. Wilkinson, N. B. Ananjeva, N. Üzüm, N. L. Orlov, R. Podloucky, S. Tuniyev, U. Kaya, A. M. Disi, S. Hraoui-Bloquet, R. Sadek, V. Tok, I. H. Ugurtas, M. Sevinç, I. Haxhiu, L. Borkin, A. Shestapol, T. Dujsebayeva, E. Golynsky, M. Chirikova, D. Nuridjanov, in *The IUCN Red List of Threatened Species*, International Union for Conservation of Nature, Gland, Switzerland **2021**.
[30] W. R. Branch, K. Howell, W. Ngalason, C. A. Msuya, in *The IUCN Red List of Threatened Species*, International Union for Conservation of Nature, Gland, Switzerland **2021**.
[31] I. J. Hagen, P. Harlow, A. Allison, A. Hamilton, O. Tallowin, in *The IUCN Red List of Threatened Species*, International Union for Conservation of Nature, Gland, Switzerland **2021**.
[32] G. Shea, in *The IUCN Red List of Threatened Species*, International Union for Conservation of Nature, Gland, Switzerland **2017**.
[33] C. Sanderson, R. Lloyd, M. Craig, G. Gaikhorst, in *The IUCN Red List of Threatened Species*, International Union for Conservation of Nature, Gland, Switzerland **2017**.
[34] J. D. Currey, in *Bones: Structure and Mechanics*, Princeton University Press, Princeton, NJ, USA **2002**.f
[35] I. Towle, A. S. Salem, A. Veneziano, C. Loch, *Arch. Oral Biol.* **2023**, *153*, 105752.
[36] M. Vickaryous, C. Williams, G. Willan, A. Kirby, A. Herrel, L. Kever, M. Moazen, A. Marghoub, S. Rai, A. Abzhanov, S. Evans, *FASEB J.* **2022**, *36*.
[37] A. Kirby, M. Vickaryous, A. Boyde, A. Olivo, M. Moazen, S. Bertazzo, S. Evans, *J. Anat.* **2020**, *236*, 1035.
[38] D. D. Beck, A. Ramirez-Bautista, *J. Herpetol.* **1991**, *25*, 481.
[39] G. W. Schuett, K. H. Peterson, A. R. Powell, J. D. Taylor, J. R. Alexander, A. K. Lappin, *R. Soc. Open Sci.* **2023**, *10*, 221466.
[40] R. Saulnier Masson, K. Daoues, J. Measey, A. Herrel, *Biol. J. Linnean Soc.* **2023**, *140*, 58.
[41] R. Ebel, A. Herrel, T. M. Scheyer, J. S. Keogh, *J. Zool.* **2025**, *325*, 1.
[42] T. M. Litchfield, Y. Ishikawa, L. N. Y. Wu, R. E. Wuthier, G. R. Sauer, *Calcif. Tissue Int.* **1998**, *62*, 341.
[43] B. R. Genge, G. R. Sauer, L. N. Wu, F. M. McLean, R. E. Wuthier, *J. Biol. Chem.* **1988**, *263*, 18513.

[44] I. S. Barreto, S. Le Cann, S. Ahmed, V. Sotiriou, M. J. Turunen, U. Johansson, A. Rodriguez-Fernandez, T. A. Grünewald, M. Liebi, N. C. Nowlan, H. Isaksson, *Adv. Sci.* **2020**, *7*, 2002524.
[45] H. Dejea, D. B. Raina, I. Silva Barreto, K. Sharma, Y. Liu, D. Ferreira Sanchez, U. Johansson, H. Isaksson, *Acta Biomater.* **2023**, *167*, 135.
[46] A. Rodriguez-Palomo, P. A. S. Vibe, M. R. Vogel Jørgensen, H. Birkedal, *Faraday Discuss.* **2025**, *261*, 116.
[47] B. Pemmer, A. Roschger, A. Wastl, J. G. Hofstaetter, P. Wobrauschek, R. Simon, H. W. Thaler, P. Roschger, K. Klaushofer, C. Streli, *Bone* **2013**, *57*, 184.
[48] A. Roschger, J. G. Hofstaetter, B. Pemmer, N. Zoeger, P. Wobrauschek, G. Falkenberg, R. Simon, A. Berzlanovich, H. W. Thaler, P. Roschger, K. Klaushofer, C. Streli, *Osteoarthritis Cartilage* **2013**, *21*, 1707.
[49] S. Frolich, H. Birkedal, *J. Appl. Crystallogr.* **2015**, *48*, 2019.
[50] M. F. Ashby, in *Materials Selection in Mechanical Design*, Elsevier, Amsterdam, The Netherlands **2004**.
[51] Z. Liu, M. A. Meyers, Z. Zhang, R. O. Ritchie, *Prog. Mater. Sci.* **2017**, *88*, 467.
[52] A. Marghoub, L. Kéver, C. J. A. Williams, A. Abzhanov, M. Vickaryous, A. Herrel, S. E. Evans, M. Moazen, *Anat. Rec.* **2023**, *306*, 2415.
[53] A. Rodriguez-Palomo, M. S. B. Jacobsen, T. E. K. Christensen, M. R. V. Jørgensen, I. Kantor, G. Willan, A. Herrel, A. Marghoub, M. Moazen, S. Evans, M. Vickaryous, C. J. A. Williams, H. Birkedal, *Acta Biomaterialia* **2025**, *204*, 457.
[54] B. Henrich, A. Bergamaschi, C. Broennimann, R. Dinapoli, E. F. Eikenberry, I. Johnson, M. Kobas, P. Kraft, A. Mozzanica, B. Schmitt, *Nucl. Instrum. Methods Phys. Res., Sect. A* **2009**, *607*, 247.
[55] A. B. Jensen, T. E. K. Christensen, C. Weninger, H. Birkedal, *J. Synchrotron Radiat.* **2022**, *29*, 1420.
[56] A. C. Larson, R. B. Dreele, in *General Structure Analysis System (GSAS)*, Los Alamos National Laboratory, Los Alamos, NM, USA **2000**, pp, 86–748.
[57] V. A. Solé, E. Papillon, M. Cotte, P. Walter, J. Susini, *Spectrochim. Acta Part B: Atomic Spectrosc.* **2007**, *62*, 63.
[58] W. C. Oliver, G. M. Pharr, *J. Mater. Res.* **1992**, *7*, 1564.
[59] E. Menendez-Proupin, S. Cervantes-Rodriguez, R. Osorio-Pulgar, M. Franco-Cisterna, H. Camacho-Montes, M. E. Fuentes, *J. Mech. Behav. Biomed. Mater.* **2011**, *4*, 1011.
[60] E. F. Morgan, G. U. Unnikrisnan, A. I. Hussein, *Annu. Rev. Biomed. Eng.* **2018**, *20*, 119.